

## ADVANCED NEUTRON ABSORBERS FOR SPENT FUEL APPLICATIONS

Galen R. Smolik, D. J. Branagan Eric L. Shaber  
(208) 526-8317 (208) 526-4674 (208) 526-8145  
Idaho National Engineering and Environmental Laboratory  
P.O. Box 1625, Idaho Falls, Idaho 83415-2218

### ABSTRACT

Neutron absorbers will play an important role in the long-term storage of certain types of enriched spent nuclear fuels. High neutron absorbing capability, long-term stability, and the capacity to stay with the fuel are important criteria in preventing critical conditions during possible waste package degradation in geological time frames. Gadolinium contained within a relatively insoluble compound or alloy is attractive from both a cost and a neutron absorbing standpoint. This paper addresses studies involving the inclusion of gadolinium in several alloy systems which have been processed to yield amorphous, nanocrystalline, or microcrystalline microstructures which provide good homogeneity and corrosion resistance.

### I. INTRODUCTION

Some lanthanides such as gadolinium (48,800 barns), europium (4,570 barns) or samarium (5,600 barns), have neutron absorption cross sections which are higher than B (760 barns) or even  $^{10}\text{B}$  (3,800 barns), which makes materials containing lanthanide elements potentially attractive neutron absorbers. Additionally, whereas isotopic separation increases the cost of  $^{10}\text{B}$  to several \$1000 per Kg, the technological demand leading to increased usage of these 'rare earth' elements have reduced the cost of these metals to \$25-40 per Kg. Currently available neutron absorbing materials are based on boron modifications of austenitic stainless steels. The boron addition is limited to about 3 wt percent due to decreases in ductility and weldability of these alloys. Solutions at a repository may range from highly acidic to alkaline depending upon the components loaded into packages, radiolytic species formed, and extent of degradation under geological time frames. Recently, the long term viability of these borated alloys has been questioned due to reduced corrosion resistance and loss of boron by leaching during long-term exposures in highly acidic solutions projected for Yucca Mountain.<sup>1</sup> The above issues promoted this investigation on

developing alternate neutron absorbing alloys containing gadolinium.

Rapid solidification processing is currently being used to process rare earth transition metal systems such as  $\text{Nd}_2\text{Fe}_{14}\text{B}$  since the rapid cooling rates result in the development of nanoscale microstructures with superior magnetic properties.<sup>2</sup> Also, metallic glasses are a class of materials which have been explored for improved corrosion resistance. These materials form during the rapid solidification of favorable alloy systems containing sufficient amounts of both metallic and metalloid elements with significantly different atomic radii. These amorphous materials have the structure of supercooled liquids with the absence of 2-dimensional defects such as grain or phase boundaries. Potentially, amorphous materials can have good corrosion resistance since sites for anodic attack are minimized. There have been several reviews relating both the roles of amorphous structure and chemical compositions to electrochemical resistance.<sup>3-6</sup> Kishitake, et al<sup>7</sup>, demonstrated that amorphous powders of Fe-11Cr-13P-8.4C-0.8Si (at%) could be produced by gas atomization and sprayed by several methods to retain various degrees of noncrystallinity. These sprayed deposits were more resistant to electrochemical attack than that of wrought 316L stainless steel as shown in Fig. 1.

Current advances in various areas of material science led us to initiate our studies incorporating Gd into various alloys systems. The objective is to incorporate the elements into a noble base material either as a dissolved atom or tightly bound as a stable intermetallic phase. We selected noble base alloys which were iron based (pseudo stainless steels), nickel based (pseudo C-22), or copper-nickel based (pseudo Monel). To these base alloys 1 and 8 at% of Gd were chosen since they bracket concentrations determined relevant in criticality calculations. The microstructures of these alloys were controlled to make the scale of the microstructure as fine as possible and in some cases, amorphous. The alloys were characterized structurally, thermally, optically, and by scoping corrosion tests.

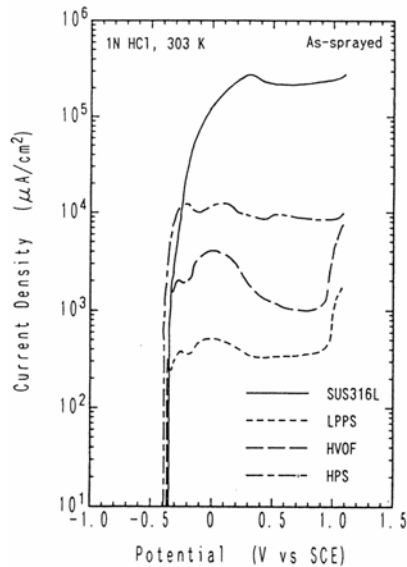


Fig. 1. Polarization curves from amorphous coatings of Fe-10Cr-13P-7C and wrought 316L stainless steel.<sup>7</sup>

## II. DESCRIPTION OF EXPERIMENTAL ALLOYS

A summary of targeted compositions of the studied alloys is given in Table 1. Series A alloys with 1 and 8 at% Gd and about 20 at% boron were designed to provide alloys with low critical cooling rates for metallic glass formation. Series B alloys were similar except they contained chromium contents comparable to the level found in stainless steels. Series D alloys had compositions comparable to Monel 400 (70Ni-30Cu) but with 1 and 8 at% Gd. The Series F alloys were designed from a highly corrosion resistant nickel-base alloy; C-22. The alloys in Table 1 were first made by melt-spinning since it allows solidification at high cooling rates (up to  $10^6$  K/s). In melt-spinning, after induction melting 15 gram ingots, a stream of liquid is ejected, using ultra high purity argon, onto a rapidly spinning copper wheel. Due to thermal contraction differences, the solidified melt flies off the wheel forming ribbons 1 to 1.5 mm wide and 25 to 40  $\mu\text{m}$  thick depending upon the alloy composition and viscosity. Subsequently, powders were made of selected alloys (10 lb melts) using inert gas atomization. During atomization, pressurized argon gas is used to break-up a molten melt stream into fine particles which solidify in flight. The spherical powders were subsequently screened to provide size distributions (typically 30  $\mu\text{m}$  mean size) and powders for characterization.

## III. CHARACTERIZATION OF ALLOY PRODUCTS

Ribbon and powder samples of the various alloys were examined using differential thermal analyses (DTA). This

technique can reveal exothermic releases as a material is heated through a transition point such as an amorphous to crystalline phase change. Examples of DTA scans for the Series B ribbons containing 1 and 8 at% Gd are shown in Fig. 2. The alloy with 1 at% Gd exhibited the glass to crystalline transition at 540°C and the 8 at% Gd alloy crystallized at higher temperatures of 660 to 680°C.

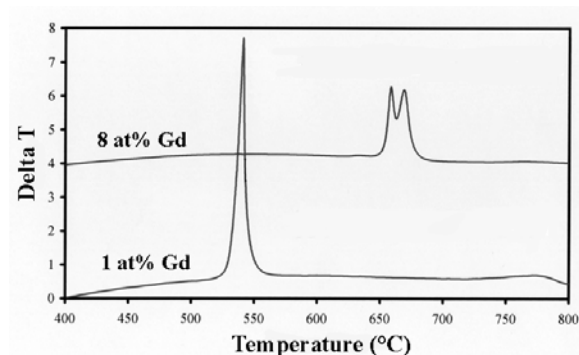


Fig. 2 DTA plots for the Series B ribbons containing 1 and 8 at% gadolinium were identified for spectra showing distinct diffraction peaks using Rietveld analysis.

X-ray diffraction (XRD) patterns for the small powder particles ( $< 20 \mu\text{m}$ ) for these two alloys are shown in Fig. 3. The broad amorphous hump and lack of Bragg diffraction peaks additionally show that powder particles of this size are amorphous.

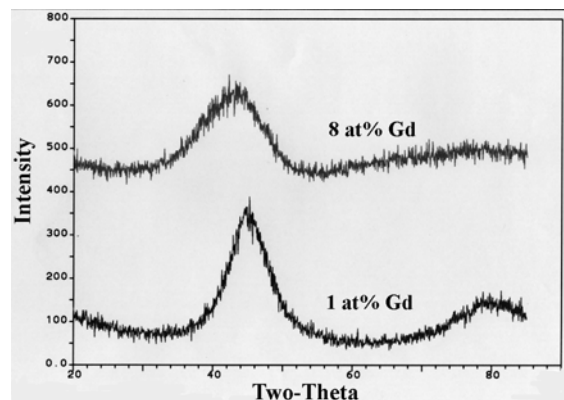


Fig. 3 XRD patterns showing dispersed peaks for the fine ( $< 20 \mu\text{m}$ ) powders for Series B alloys.

The DTA curves in Fig. 2 show that the higher Gd content actually promoted glass forming ability in the Series B alloy. XRD of the fine powders of the other alloys revealed whether they were amorphous or crystalline as

indicated in Table 2. Studies were additionally launched to determine where Gd was residing. For all of the alloys with 1 at% Gd addition, the Gd containing phase was not detected in the XRD scans. In the series A and B alloys, the Gd is dissolved as an atom in the glass structure. Phase identification after stress relieving at 800°C was done on selected alloys containing 8 at% Gd using X-ray diffraction scans followed by detailed Rietveld refinement. In the Series B alloy after crystallization, the Gd resided in the tetragonal  $Gd_2Fe_{14}B$  phase, in the hexagonal  $Gd_2Ni_{17}$  phase in the Series D alloy, and in the hexagonal  $GdNi_5$  phase in the Series F alloy (see Table II).

Metallographic cross sections were also prepared from the rapidly solidified products. The very fine microstructural features in Series F ribbon with 1 at% Gd are revealed with scanning electron microscopy (SEM) in Fig. 4. There is a gradient in structure across the ribbon. The structure near the wheel surface is too fine to be resolved. The size of microstructural features progressively increase across the cross section of the ribbon to about 1  $\mu m$  at the outer surface.

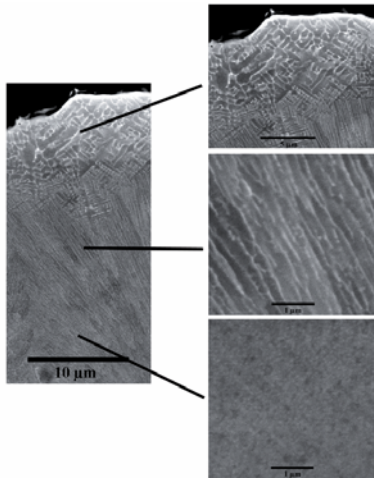


Fig. 4. SEM showing the very fine microstructures in ribbon of the Series F alloy with 1 at% gadolinium.

SEM was also used to reveal the microstructures in the gas atomized powder particles. Examples are shown for small (<20  $\mu m$ ) and larger particles (75-100  $\mu m$ ) for the series B, D and F alloys in Fig. 5 and Fig. 6 respectively. Both of Series B powders in Fig. 5 show the featureless conditions of a metallic glass which agrees with the DTA and XRD results. The Series F powders show features consistent with nucleation and growth during solidification. The dendrite arm spacing in the APMF1 powder is about 1  $\mu m$  which is quite similar to that at the outer surface for the ribbon.

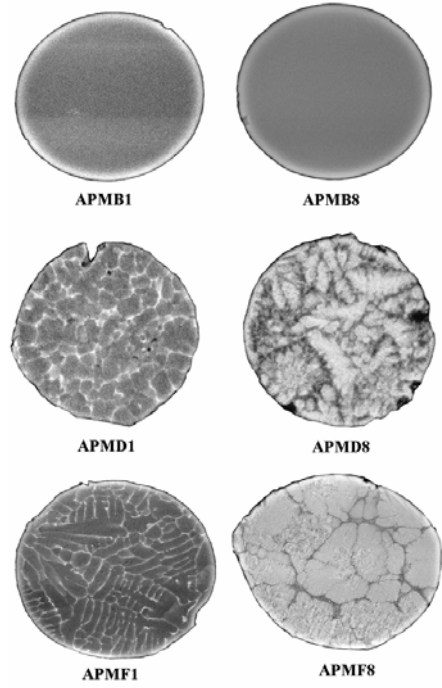


Fig. 5 Microstructures in as-atomized 10-20  $\mu m$  powder particles of Series B and Series F alloys with 1 and 8 at% Gd, respectively. Magnification:  $\approx 2000X$ .

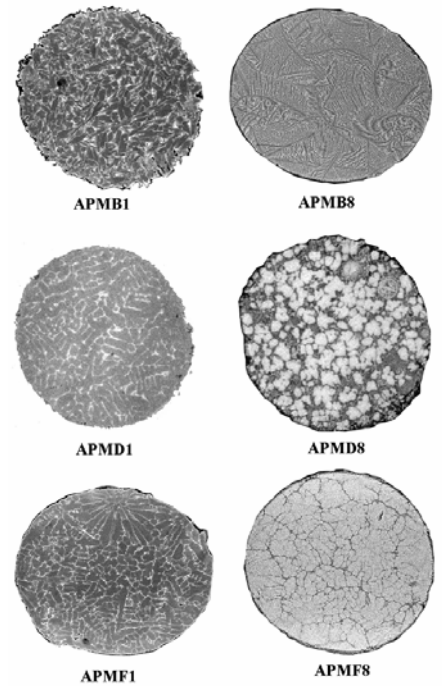


Fig. 6 Microstructures in as-atomized 75-100  $\mu m$  powder particles of Series B and Series F alloys with 1 and 8 at% Gd, respectively. Magnification:  $\approx 400X$ .

Microstructural features were even finer in the APMF8 powder which had an interlamellar spacing of 100 nm (Fig. 7). The larger 75-100  $\mu\text{m}$  particles of all alloys all cooled slowly enough to have solidified with crystalline microstructures. The slower cooling rates for the larger particles of Series B alloys resulted in a quite different structure (almost eutectic for APMB8) as the mode changed from amorphous to crystalline. Microstructures for the larger Series F particles on the other hand are quite similar to smaller particles with the same Gd content with similar dendrite arm spacing and grains sizes.

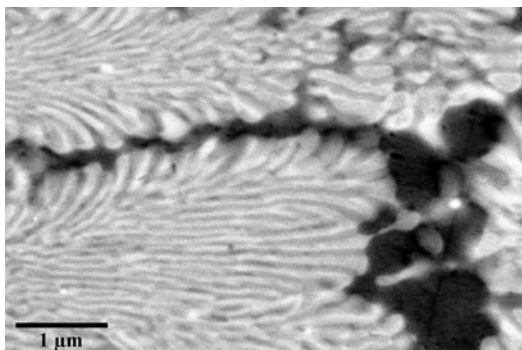


Fig. 7 SEM micrograph of the Series F alloy with 8 at% Gd. The extremely fine pearlitic type microstructure is shown with an interlamellar spacing of 100 nm.

#### IV. CORROSION TESTS OF RIBBON PRODUCTS

Samples of melt spun ribbons were corrosion tested in a solution of a modified Yucca Mountain J13 well water. Well J13 is located near Yucca Mountain, AZ, the site currently being investigated for use as a national repository for spent nuclear fuel. The ribbons samples were tested under conditions used for other corrosion tests for the Yucca Mountain Project.<sup>1</sup> This included a 96-hour exposure in a 90°C A solution with the following composition to simulate radiolytic and mineral effects: 0.01 M formic acid (HCOOH), 0.01 M sodium formate (NaCOOH), 0.02 M sodium oxalate ( $\text{Na}_2\text{C}_2\text{O}_4$ ), 0.01 M nitric acid ( $\text{HNO}_3$ ), 0.01 M sodium chloride (NaCl), and 0.01 M hydrogen peroxide ( $\text{H}_2\text{O}_2$ ) in distilled water. Ribbon samples of 0.5 to 1.0 gram were suspended in solution in porous, chemically resistant, polyethylene bags. The bags and samples were thoroughly washed with distilled water after exposure. It was hoped that the weight changes could be corroborated with corrosion but moisture adsorption by the bag container prevented meaningful weight gain data from being obtained. However, the ribbon samples were examined by various methods and the solutions were analyzed with inductive coupled plasma-atomic emission spectroscopy (ICP-AES).

The visual appearance of the ribbons provided first hand information about the resistance of the various alloys in the rather aggressive solution having a pH of about 3.5. The Series A alloys with Fe-B-Gd showed significant attack and reddish colored iron oxide. The B series alloys with chromium generally retained their shiny appearance although small areas of a reddish oxide formed at isolated contact points between pieces of ribbons. The alloy with 8 at% Gd, APMB8, showed fewer of these initiation sites. Series D alloys based on Cu-Ni were generally severely attacked by this environment. Interestingly, APMD8 with 8 at% Gd showed better resistance than its counterpart with 1 at% Gd. A significant portion of the ribbons still retained their shiny appearance. No evidence of attack was apparent for the 1 and 8 at% Gd Series F alloys based on the Alloy C-22 composition as both ribbons remained quite shiny.

SEM examinations of the pretest and exposed ribbons provided additional information. Corrosion products identified with energy dispersive spectroscopy (EDS) showed that the corrosion products on the Series D alloys were basically oxides with a formula of  $(\text{Ni,Cu})\text{O}$ . EDS analysis of a non-reacted area on APMD8 showed only a slight pick-up of oxygen, 0.15 at% and the Ni, Cu, and Gd concentrations were 61.7 at%, 26.0 at%, and 10.8 at% respectively, which is close to the targeted composition in Table 1. Areas of corrosion products on the Series B contained primarily iron and chromium with up to 15 at% oxygen and lesser amounts of sodium and chloride. Analysis from a non-reacted shiny area on the APMB8 showed 2.2 at% O, 68.8 at% Fe, 17.3 at% Cr, and 11.8 at% Gd which is also close to the targeted composition (boron was not detected in the EDS). SEM images of the top surface of the APMF8 ribbon before and after exposure to the corrosion environment are shown in Fig. 8. No influence such as pitting or localized attack is apparent. The EDS analyses are also very similar for the pre-exposed and corrosion tested ribbons; i.e., Ni-55.4 at%, Cr-23.2 at%, Gd-10.5 at%, Mo-6.0 at%, and Fe-3.2 at%. In the exposed ribbon, an additional 3.0 at% (0.7 wt%) oxygen was measured, indicating a thin oxide did form.

Auger electron spectroscopy (AES) was used to obtain surface analyses and depth profiles by sputtering on selected especially corrosion resistant alloys. Depth profiles for various elements for the as-spun and corrosion tested ribbons of APMF8 are shown in Fig. 9. Surface analyses showing the atomic concentrations before and after sputtering are in Table 3. Results for the pre-exposed and corrosion tested conditions are very similar. Analyses show that before sputtering there is a substantial oxygen peak. There are enrichments of Gd of about 18 at% associated with this oxide layer. This is substantial higher than the 9 to 11 at% measured by EDS, which provides analyses to a

greater depth. The AES surface analyses for nickel, chromium, molybdenum, and iron are all lower than those measured with EDS analyses. These analyses and the profiles in Fig. 9 show that a thin Gd oxide layer exists on both the as-spun and corrosion tested ribbons. The oxide layer apparently formed upon solidification during melt-spinning. A higher concentration of carbon was the only significant difference observed on the corrosion-tested ribbon. The AES analyses of the APMF8 alloys approached the bulk composition after sputtering for 20-30 minutes. AES analyses for APMF1 with 1 at% targeted Gd showed some similar trends with an initial oxide layer of nearly 12 at% Gd. The concentration of Gd decreased with sputtering to a level below the detection limit by AES. This could perhaps reflect a depletion zone caused by Gd diffusing rapidly to the surface during cooling. If this indeed is a depletion zone, this could indicate that a more substantial Gd oxide layer forms on the 8 at% Gd-bearing alloys. This condition and the observation of better corrosion resistance on several of the alloys containing the higher Gd contents suggests that the oxide layers provided some protection during corrosion testing. The extent of this protection needs to be proven with longer-term tests.

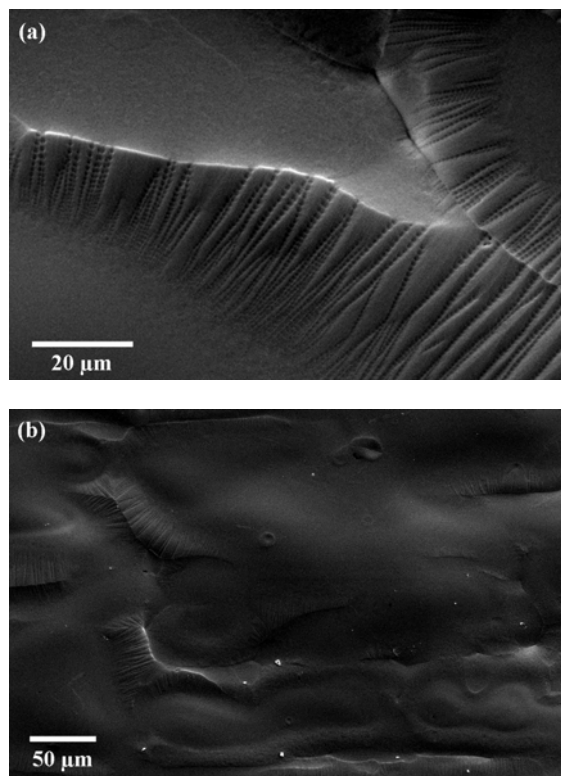


Fig. 8 SEM images of Series F ribbons with 8 at% Gd. (a) As-spun. (b) Corrosion tested.

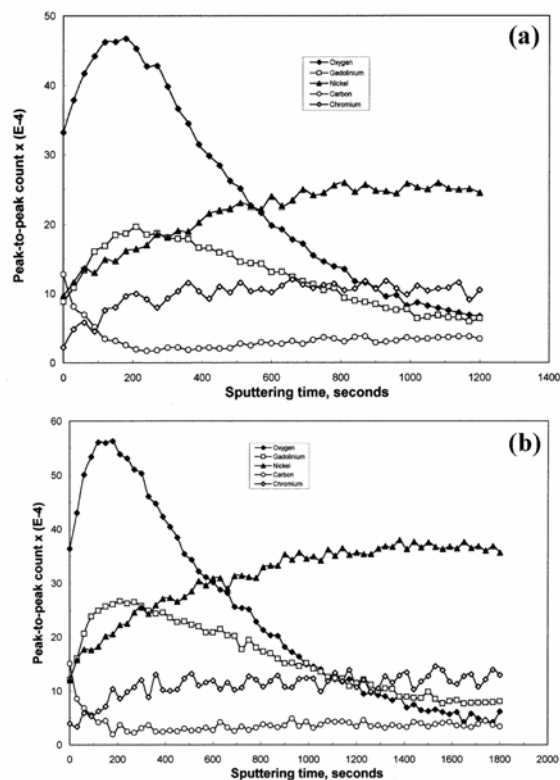


Fig. 9 AES depth profiles of various elements for APMF8 ribbon. (a) As-spun, (b) Corrosion tested.

The 700-ml solutions used to test the ribbon samples were analyzed by ICP-AES. The solutions included the water used to thoroughly rinse the samples and the bag in which they were contained. The solutions were filtered through a Millipore 0.2-0.6  $\mu\text{m}$  glass fiber filter. Chemical analysis was determined for both the filtrates and the dissolved filters. The analyses from these two sources have been combined to provide the total quantities ( $\mu\text{g}$ ) for the various elements in a particular test. The quantities for Fe, Gd, and Ni for selected tests are listed in Table 4. We expect that some iron ( $\approx 40 \mu\text{g}$ ) could be from the dissolved glass fiber filter. The measurements of low Fe and Gd for APMB8 correlate with the sample visually showing better corrosion resistance. Similar correlations exist for the nickel-base APMD1 and APMD8 alloys. The highly corrosion resistance Series F alloys showed no detectable Gd dissolution.

## V. DISCUSSION AND CONCLUSIONS

Results from the iron base Series A alloys show that achieving an amorphous condition is not in itself sufficient to give good corrosion resistance. The composition is also important as shown by the Series B alloys which were also

amorphous but contained Cr and Gd and which displayed much higher corrosion resistance. This is in agreement with published data showing that the presence of passivating elements are also necessary for good corrosion resistance.<sup>5,6</sup> The modified Alloy C-22 showed excellent corrosion resistance in the rapidly cooled ribbon which can be attributed to be the result of a favorable composition coupled with the extremely fine scale of the microstructure.

Auger electron spectroscopy showed that thin oxide layers enriched in Gd formed on the melt spun ribbons during cooling or while exposed to air at ambient temperature. The Series F alloy simulating C-22 with 1 at% Gd showed an enrichment of 12 at% Gd on the as-spun surface. Sputtering showed this oxide layer to be very thin and possible accompanied with an underlying zone with Gd depletion. Series B and F alloys with 8 at% Gd had surface enrichments of 16 to 18 at% Gd. Sputtering with depth profiling showed that the outermost oxide layers on these alloys were enriched in Gd rather than Cr. Sputtering did not show indications of depletions in Gd but rather a decreasing trend toward the base metal composition. Preference of Gd<sub>2</sub>O<sub>3</sub> formation over that of Cr<sub>2</sub>O<sub>3</sub> would be expected based upon a larger negative heat of formation for the gadolinium oxide, i.e., -434 kcal/mole compared to -253 kcal/mole. This meets one criteria suggesting that a Gd-enriched oxide layer may provide protection in the rather aggressive acidic solution. Another rare earth element, cerium, has been used for improving high temperature oxidation resistance. The improvements are postulated as the result of anchoring the oxide scale preventing spalling or oxide modifications which influence diffusional process across the oxide scale.<sup>8,9</sup> Cerium applications have also been used for corrosion inhibition in low temperature aqueous environments.<sup>10,11</sup> A beneficial factor in the rapidly solidified alloys is that their very fine microstructures result in a decreased required diffusion distance. This enhances Gd enrichment in the oxide surface and hence its ability to assist in passivating the surface.

To date we have demonstrated that good corrosion resistance can be obtained from melt-spun ribbons of selected alloys. The corrosion resistance varies sensitively to both the composition and the microstructure at the surface. Our best results have been from nickel base alloys similar to C-22. These results have been achieved in alloys with multiphase, crystalline material with very fine features. To realize the potential of Gd-bearing alloys for neutron absorbers product scale-up and engineering applications need to be demonstrated. This requires a sufficient knowledge of correlations between chemistry control, microstructural features and corrosion behavior, as well as how these factors are influenced by processing conditions such as the cooling rate. We are exploring various methods

of consolidation including hot extrusion and spraying processes, viz., low-pressure plasma spraying and high-velocity oxyfuel spraying. Such consolidation methods will enhance the type of products and applications for use in the handling of enriched spent fuels.

#### ACKNOWLEDGEMENTS

The authors wish to thank their associates whom have helped in this study. The melt spun ribbons were produced at the Materials Preparation Center at Ames Laboratory. Joe Burch has designed and run the atomization system producing the powders and Eliz Richman provided characterization of the various products at the INEEL. We thank Evan Hales for performing the corrosion tests and Marilyne Tsang and Byron White for assisting in the chemical analyses. Todd Morris has provided assistance with metallographic preparations and Mike Hankins has performed the SEM and AES. We also thank other associates at the INEEL, especially Henry Loo and Larry Taylor, for their helpful input regarding criticality issues in various types of spent fuels.

#### REFERENCES

- [1] R.A. Van Konynenburg et al., Scoping Corrosion Tests on Candidate Waste Package Basket Materials for the Yucca Mountain Project, UCRL-ID-13086, (1998).
- [2] J.F. Herbst, "R<sub>2</sub>Fe<sub>14</sub>B Materials: Intrinsic Properties and Technological Aspects", 63 (1991), 819-898.
- [3] T.K.G. Namboodhiri, "Corrosion Resistance and Applications", in *Metallic Glasses Production, Properties and Applications*, ed. by T.R. Anantharaman, Trans Tech Publications, pp. 203-223 (1984).
- [4] R.G. Kelly and R.C. Newman, "Advanced Materials: Corrosion and Electrochemistry", in *Electrochemical and Optical Techniques for the Study and Monitoring of Metallic Corrosion*, ed. by M.G.S. Ferreira and C.A. Melendres, Kluwer Academic Publishers, pp.665-696 (1991).
- [5] K. Hashimoto and T. Masumoto, "Corrosion Behavior of Amorphous Alloys", in *Treatise on Material Science and Technology*, 20, Academic Press Inc., pp. 291-324 (1981).
- [6] M. Janik-Czachor, "Passivity of Metal-Metalloid Glasses", *Corrosion Science*, 31, pp. 325-332 (1990).

- [7] Kishitake et al., “Thermal Sprayed Fe-10Cr-13P-7C Amorphous Coatings Possessing Excellent Corrosion Resistance”, *J. of Thermal Spray Technology*, 5, pp. 476-482 (1996).
- [8] S. Seal et al., “Improvements in the Oxidation Behavior of Austenitic Stainless Steels by Superficially Applied, Cerium Oxide Coatings” *Oxidation of Metals*, 41, pp. 139-178 (1993).
- [9] F. Czerwinski and W.W. Smeltzer, “The Growth of Thin Oxide Films on Ceria-Sol-Coated Nickel”, *Oxidation of Metals*, 40, pp. 503-527 (1993).
- [10] Y.C. Lu and M.B. Ives, “Chemical Treatment with Cerium to Improve the Crevice Corrosion Resistance of Austenitic Stainless Steels”, *Corrosion Science*, 37, pp. 145-155 (1995).
- [11] H.S. Isaacs and A.J. Davenport, “The Electrochemical Response of Steel to the Presence of Dissolved Cerium”, *J. Electrochem. Soc.*, 138, pp. 390-393 (1991).

**Table 1 Alloy Composition**

Alloy	Composition (at%)
APMA1	(Fe <sub>0.8</sub> B <sub>0.2</sub> ) <sub>99</sub> Gd <sub>1</sub>
APMA8	(Fe <sub>0.8</sub> B <sub>0.2</sub> ) <sub>92</sub> Gd <sub>8</sub>
APMB1	[(Fe <sub>0.8</sub> Cr <sub>0.2</sub> ) <sub>0.8</sub> B <sub>0.2</sub> ] <sub>99</sub> Gd <sub>1</sub>
APMB8	[(Fe <sub>0.8</sub> Cr <sub>0.2</sub> ) <sub>0.8</sub> B <sub>0.2</sub> ] <sub>92</sub> Gd <sub>8</sub>
APMD1	(Ni <sub>0.7</sub> Cu <sub>0.3</sub> ) <sub>99</sub> Gd <sub>1</sub>
APMD8	(Ni <sub>0.7</sub> Cu <sub>0.3</sub> ) <sub>92</sub> Gd <sub>8</sub>
APMF1	*(C-22) <sub>99</sub> Gd <sub>1</sub>
APMF8	*(C-22) <sub>92</sub> Gd <sub>8</sub>

\*C-22 = Ni<sub>63.0</sub>Cr<sub>24.6</sub>Mo<sub>8.2</sub>Fe<sub>3.3</sub>W<sub>0.7</sub>V<sub>0.2</sub>

**Table 2 Rietveldt Analysis of Gd Containing Phases After Heat Treating at 800°C**

Alloy	Phase	Space Group	Lattice Parameters (Å)
APMB8	Gd <sub>2</sub> Fe <sub>14</sub> B	P4 <sub>2</sub> /mnm	a = 8.744 c = 12.042
APMD8	Gd <sub>2</sub> Ni <sub>17</sub>	P6 <sub>3</sub> /mmc	a = 8.371 c = 8.126
APMF8	GdNi <sub>5</sub>	P6/mmm	a = 4.904 c = 4.006

**Table 3 AES Surface Analyses of Ribbons (at%)**

APMF1 (as-spun)	Initial	Final
O	21.86	14.09
C	35.13	13.34
Ni	17.45	48.94
Gd	11.68	*n.d.
Cr	8.49	11.74
Mo	4.57	7.24
Fe	*n.d.	*n.d.
N	17.45	4.68
APMF8 (as-spun)	Initial	Final
O	31.01	10.46
C	18.57	11.15
Ni	16.70	41.18
Gd	17.76	11.00
Cr	11.34	14.86
Mo	1.24	6.48
Fe	1.74	2.35.
N	1.64	2.53
APMF8 (corrosion tested)	Initial	Final
O	27.66	7.37
C	24.81	8.18
Ni	17.46	45.95
Gd	17.74	13.49
Cr	9.92	12.52
Mo	2.40	6.84
Fe	*n.d.	2.54.
N	*n.d.	3.11

\* not detected

**Table 4 Elemental Losses From Corrosion Tests ( $\mu\text{g}$ )<sup>a</sup>**

<b>Alloy</b>	<b>Fe</b>	<b>Gd</b>	<b>Ni</b>
APMA1	11,027	358	8
APMA8	965	583	15
APMB1	1,722	41	8
APMB8	93	3	14
APMD1	126	1142	8,534
APMD8	114	5	18
APMF1	58	* n.d.	44
APMF8	232	* n.d.	10

<sup>a</sup> Losses measured from 0.5-1.0 g samples.

The detection limit for Gd is about 1  $\mu\text{g}$ .

\* not detected